Journal of Materials Research and Technology 30 (2024) 7621–7634

Contents lists available at ScienceDirect

Journal of Materials Research and Technology

journal homepage: www.elsevier.com/locate/jmrt

Correlation between pulse frequencies, microstructure and mechanical properties of TA15 in wire and arc additive manufacturing

Zhenyu Yu [a,b,c], Shengfu Yu [a,b,*], Guozhi Yu [a,b], M.W. Fu [c,**]

[a] School of Materials Science and Engineering, Huazhong University of Science and Technology, Wuhan, PR China
[b] State Key Laboratory of Materials Processing and Die & Mould Technology, Huazhong University of Science and Technology, Wuhan, PR China
[c] Department of Mechanical Engineering, Research Institute for Advanced Manufacturing, The Hong Kong Polytechnic University, Hong Kong, PR China

ARTICLE INFO

Handling editor: L. Murr

Keywords:
Pulse frequency
Wire and arc additive manufacturing
Titanium alloy
Microstructure
Mechanical property

ABSTRACT

Wire and arc additive manufacturing (WAAM) has been developed to be a highly efficient technique for making large Ti-alloy products. However, the deposition of metal by this method causes coarse texture, which limits its application. To address this, the study utilizes a wire and pulsed arc additive manufacturing (WPAAM) process for making TA15 alloy. Compared with the WAAM method, this WPAAM method inducts several current/voltage-impulse cycles under different pulse frequencies, which makes grains tiny and improves tensile strength. The study then uses a VOF model to discuss the effect of impulse cycles on the solidification process. The findings suggested that the impulse cycles deform the molten pool and influence the vibration in the solid/liquid interface. This makes the coarse columnar grains tiny and forms diminutive α laths. This paper further discusses the correlation between the microstructure and the mechanical properties. The results show that the CBGs and the α laths play a joint contribution to yield strength in the WAAMed TA15 alloy. This study provides a reference for optimizing the microstructure of WAAM titanium alloys by adjusting pulse frequencies and provides a theoretical basis for strengthening WAAMed Ti-alloy.

1. Introduction

Titanium alloys (Ti-Alloys) have been widely used in various fields and industrial clusters, particularly in aeronautical and aerospace industries. However, the limited processability restricts its utilization. Specifically, the parts and components in aeronautical and aerospace industries are predominantly thin-wall structures to meet weight reduction requirements [1]. As a result, nearly 80% of the materials are cut off during machining, resulting in significant waste [2]. To address this issue, wire and arc additive manufacturing (WAAM) technology was proposed and developed as an efficient method for making Ti-alloy products [3]. Recent reports have highlighted and recommended using WAAM technology to manufacture large metallic components [4–6], particularly in the aeronautical and aerospace industries.

Foremost among the merits inherent to WAAM is its commendable high-deposition rate. This is predicated upon a substantial heat input requisite for the wire's melting. However, the augmentation in heat input inevitably precipitates a notable accumulation of thermal energy. This heat accumulation, in turn, produces a proclivity for microstructural coarsening [3,7]. From the prior articles, the printed Ti-alloy components exhibit strong solidification textures characterized by the large columnar β grains (CBGs) [8]. These coarse textures significantly affect the mechanical properties of the parts.

Certain works [9–12] point out that the grain size experiences a profound influence from the solidification conditions inherent in the manufacturing process, notably dictated by the thermal gradient (G) to the growth rate (R) ratio, commonly referred to as the G/R ratio. As a result, the larger the *G/R* ratio, the coarser grains will be produced [13–15]. In tandem with this, some scholars tried to use a specific amount of heterogeneous nucleation particles like silicon, La_2O_3, and TiC [16–18] to increase the growth rate (R). However, the alloy's modification can influence its holistic performance, which remains an unresolved aspect and is awaiting further scrutiny and determination.

In terms of the thermal gradient (G), many researchers use Cold metal transfer (CMT) technology to reduce the heat input [19,20]. The principle of the traditional WAAM is shown in Fig. 1(a). Initially, the arc is ignited upon contact between the wire and the substrate, followed by controlled withdrawal of the wire to establish a stable arc. During this

* Corresponding author. School of Materials Science and Engineering, Huazhong University of Science and Technology, Wuhan, PR China.
** Corresponding author.
E-mail addresses: yushengfuhust@hotmail.com (S. Yu), mmmwfu@polyu.edu.hk (M.W. Fu).

https://doi.org/10.1016/j.jmrt.2024.05.149
Received 25 March 2024; Received in revised form 15 May 2024; Accepted 16 May 2024
Available online 19 May 2024

period, the current and voltage are increased rapidly and maintained in a certain level to sustain the arc. As the molten droplet gradually grows with the wire feed, it eventually contacts the substrate, forming a liquid bridge transition. Subsequently, upon wire withdrawal, there is an abrupt drop in current and voltage, marking the initiation of the next phase of the process. In the CMT process, the arc sustains a high heat input specifically during the droplet transition period, contrasting with lower heat input levels during other stages. This deliberate modulation serves to minimize the energy expended during the whole process. Although the CMT method can reduce the heat input compared to other arc additive methods [21], the heat input is still very high. The WAAMed parameters, such as current and voltage, can only be adjusted within a certain range. Otherwise, the AM process won't be stable. Thus, reducing the thermal gradient G in the magnitude order is technically difficult by regulating the WAAMed parameters.

Many scholars have used wire and pulsed arc additive manufacturing (WPAAM) to reduce the size of grains and have achieved good results in refining grains. This technology integrates pulse welding with the traditional WAAM process, incorporating multiple current/voltage-impulse cycles within a single CMT period, as depicted in Fig. 1(b). These impulse cycles make the current and voltage into an instantaneous high level, which introducing wire necking and facilitating the detachment of droplets from the wire. Consequently, the droplets descend from a certain distance onto the substrate, inducing impact in the molten pool, generating co-vibration to refine the grains. Zhuan et al. [22] use WPAAM to refine the grains in 2319 aluminum alloy and get good mechanical properties. Wang et al. [23] use WPAAM to achieve grain refinement and strengthen the deposited metal of 304 stainless steel welds. Zhang et al. [24] compare different arc modes in 5A06 alloy and find impulse cycles can refine the grains and improve the mechanical properties. However, few studies have been conducted on the microstructure and properties of titanium alloys using WPAAM technology. The effect of pulse frequency on the solidification process has rarely been studied.

This work aims to evaluate the efficacy of the wire and pulsed arc additive manufacturing process in refining the aforementioned CBGs in Ti-alloy. By changing the pulse frequency, the microstructure of the deposited metal under different parameters was obtained, and the corresponding mechanical properties were also tested. A volume of fluid (VOF) model is used to explain the mechanism of impulse cycles in the solidification process. Then, the correlation between microstructure and mechanical properties is built. With these research outcomes, this technology provides a new method for controlling the microstructure of WAAMed titanium alloy and provides a theoretical explanation for the strengthening mechanism between microstructure and mechanical properties.

2. Experiments

2.1. Materials and manufacturing process

For this study, a TA15 base plate (Huitongyi Group, Shanxi, China) is chosen for the experiment, with dimensions of 240 mm length, 180 mm width, and 14 mm thickness. The wire material is TA15 (Baotai Group, Shanxi, China), with a diameter of 1.2 mm. The chemical compositions of the wire and plate are presented in Table 1. Before the experiment, the base plates were mechanically grinded and polished to eliminate oxide films on the surface and then cleaned with acetone to remove oil or grease.

The experimental setup employed in this study was presented in Fig. 2. It comprised a 6-DOF KR30-HR robot from KUKA and a TPS 4000i CMT welding supply by Fronius. A welding tail was established to build a protective atmosphere that prevented oxidation during the process. The pure argon (99.99%) gas flow rate in the welding gun and the welding tail was maintained at 15.0 L/min and 25.0 L/min, respectively. Other corresponding parameters used in the experiments are shown in Table 2. Current and voltage waveforms in the WAAM process were acquired using a Fronius 0805 CMT expert base, specifically under expert program number DB 01-2023. The WPAAM program was derived from this expert base, incorporated with various pulsed circles under different F_p, and rewritten into the CMT period.

During the experiment, an electrical signal acquisition system comprising a current sensor and a voltage sensor was utilized to capture the current and arc voltage at a sampling rate of 50 kHz.

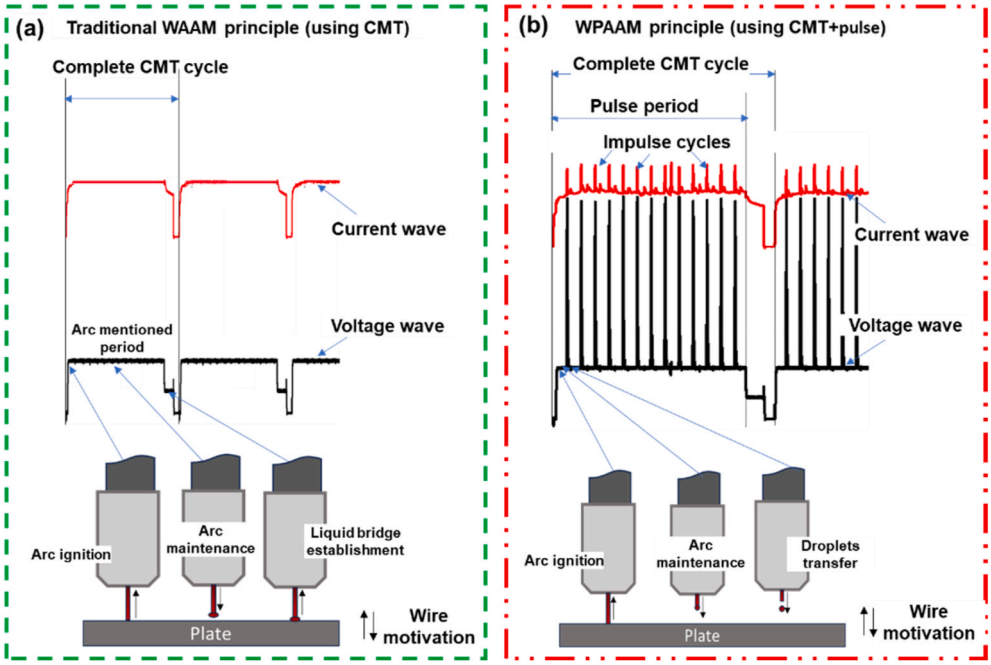

Fig. 1. The principle of the traditional WAAM and WPAAM: (a) Traditional WAAM principle and (b) WPAAM principle.

Table 1
The main chemical composition of the wire and substrate (mass fraction, %).

	Al	Mo	V	Zr	O	C	N	H	Ti
Wire	6.5	1	0.95	1.05	0.002	0.003	0.017	0.002	Bal.
Base plate	6.53	1	1.07	1	0.06	0.02	0.015	0.012	Bal.

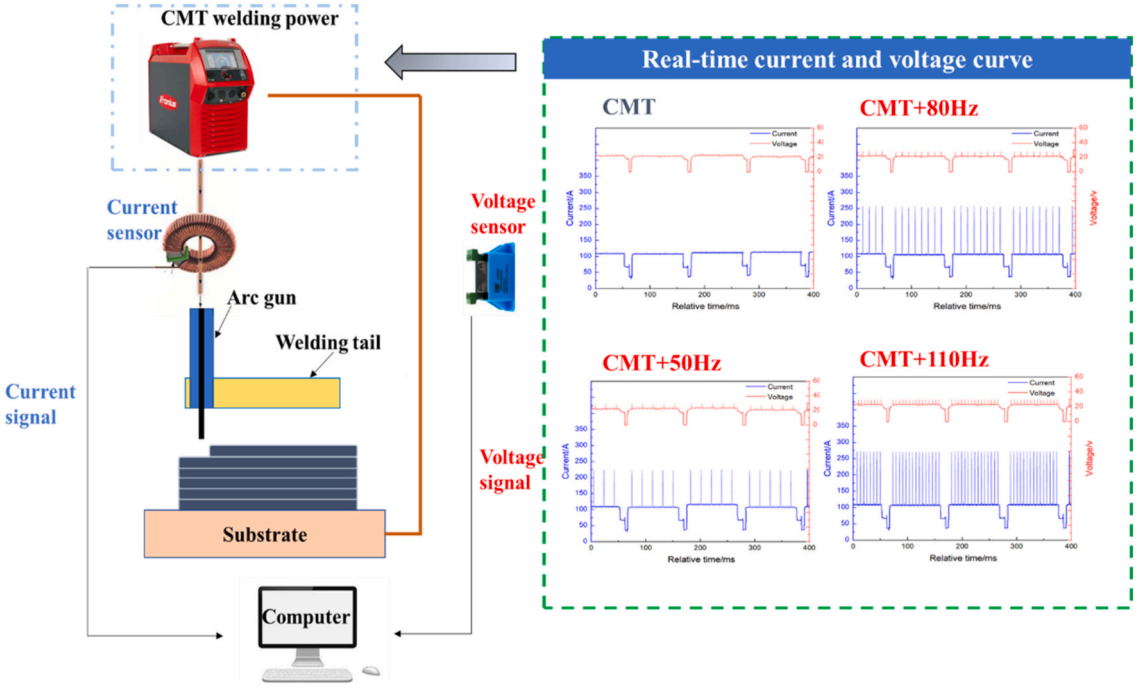

Fig. 2. Experimental setup of the WPAAM system.

Table 2
The parameters used in this study.

Sample Remarks	1	2	3	4
Pulse frequencies F_p (Hz)	0	50	80	110
Average Current (A)	122	117	115	115
Average Voltage (V)	19.3	20.5	20.6	20.0
Traveling Speed (m/min)	0.35	0.35	0.35	0.35
Wire Feeding Speed (m/min)	6.0	6.0	6.0	6.0

2.2. Characterization and mechanical testing of samples under different parameters

Metallurgical samples were cut by a wire-electrode cutting machine. These samples were then polished through SiC papers up to grid 3000 and diamond paste up to 0.5 μm. Then, the etching solution was done using Kroll's reagent (1 ml HF + 2 ml HNO_3 + 17 ml H_2O) for 1 min. The CBG morphology was examined using a KEYENCE VHX-1000C ultra-depth microscope for detailed observation. The sizes of CBGs were measured using the software Image-J. Tensile test samples were fabricated and machined according to standard GB/T 228.2–2015. The sample position in the as-built wall is shown in Fig. 3 (a). The geometries of these tensile samples are shown in Fig. 3 (b). Three tensile specimens are taken out of each straight wall for experiments. Then, these samples were conducted at room temperature with a 1 mm/min loading rate using a Zwick Z020 electronic universal tester.

The fabricated samples' grain orientation, size, and texture under different pulse frequencies (F_p) were investigated using a scanning electron microscope (SEM, Zeiss Gemini 300) equipped with an electron backscatter diffraction system (EBSD, Oxford Nordlys Max 3 system). The EBSD scans were performed on a sample area measuring 400 × 400 μm^2, with a step size of 0.5 μm.

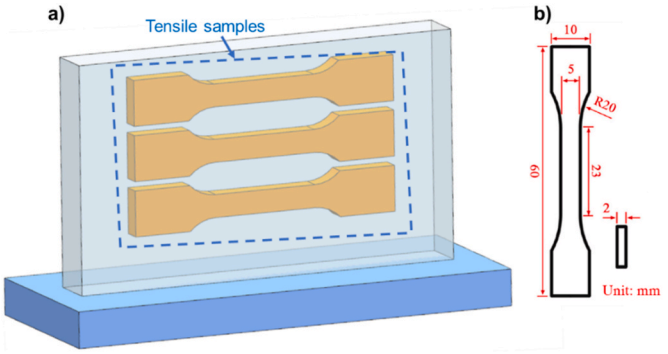

Fig. 3. Samples schematic diagram (a) Sample position in the straight wall, and (b) Tensile samples.

3. Results

3.1. Mechanical properties under different pulse frequencies

Fig. 4 presents the mechanical properties under varying F_p in the wire and pulsed arc additive manufacturing process. A comparative reference is established by including the mechanical properties under the WAAM process at 0 Hz. The yield strength (YS) and ultimate tensile strength (UTS) are quantified for this baseline at 888.48 and 985.40 MPa, respectively. The zenith of *YS* is attained at 50 Hz, registering at 1007.58 MPa, denoting a notable enhancement of 119.1 MPa (approximately a 13.4% improvement) relative to the WAAM counterpart.

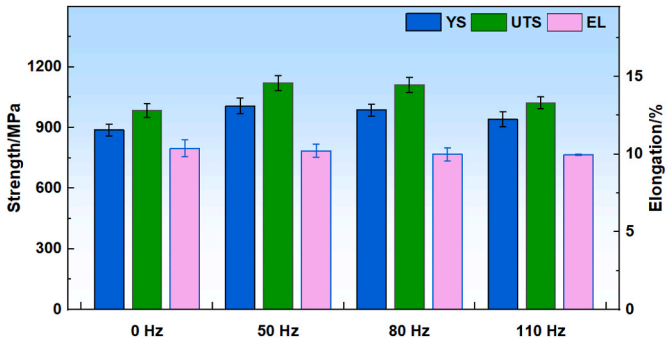

Fig. 4. The tensile test results of the WPAAMed workpieces under different F_p.

Subsequently, with escalating F_p values, the *YS* experiences a marginal decline, measuring 987.64 MPa at 80 Hz. Ultimately, at the F_p of 110 Hz, the *YS* diminishes to approximately 941.45 MPa, showcasing a 53 MPa improvement compared to the WAAM process at 0 Hz.

Similarly, the apogee of *UTS* is also realized at 50 Hz, reaching 1122.23 MPa, thereby signifying a notable augmentation of 136.84 MPa (approximately a 13.9% improvement) compared with the WAAM baseline. Subsequent increments in F_p result in a marginal decrement in *UTS*, with values of 1112.09 and 1023.31 MPa observed at 80 and 110 Hz, respectively. Overall, a conspicuous divergence is observed between specimens subjected to WAAM and those exposed to WPAAM, indicating improvements in both *YS* and *UTS* results.

The elongation exhibited by the tensile samples remains consistently uniform across varying F_p, approximating an equable magnitude of 10%. This constancy in elongation means a relative insensitivity of the deformation characteristics to alterations in F_p within the range of investigated parameters. The fractography of these samples is shown in Fig. 5, wherein the presence of a conspicuous shear lip is readily discernible. In the central region of the fractography, diminutive dimples and discernible tear ridges are manifested. In totality, the fracture modalities evidenced by these specimens evince ductile comportment, with the prevailing fracture mechanism predominantly characterized by a discernible occurrence of dimple formation.

3.2. The CBGs under different pulse frequencies

Previous studies [16,17,25–27] have consistently delineated the presence of multiple parallel coarse columnar grains (*CBGs*) in the microstructure along the build direction. These *CBGs*' widths are usually 0.5–1.1 mm. This study acquires microstructure samples perpendicular to the build direction, affording a comprehensive cross-sectional view of the deposited metal.

Fig. 6(a), (b), (c), and (d) showcase the OM images of specimens subjected to the WPAAM process, each corresponding to distinct F_p of 0, 50, 80, and 110 Hz. The *CBG* area distribution is shown in Fig. 6(e), (f), (g), and (h), respectively. The Gaussian fitting is used to evaluate these distributions' status, represented by the red lines. The accompanying confidence coefficients R^2 are quantified at 0.567, 0.972, 0.857, and 0.815, respectively. The coefficients R^2 in Fig. 6(f), (g), and (h) mean that the *CBG* areas in these samples have high robustness, fitting the Gaussian distribution.

Thus, the boxplot is used to scrutinize the impact of F_p on the distribution of the *CBGs*, as shown in Fig. 7(a). The boxplot shown in Fig. 7 (a) is constructed by the 25%–75% aligned *CBG* areas referred from the grain distribution. Two critical sectors, the mean value (M_v) and the concentration degree (C_d), are used in Fig. 7 (b) to describe the characteristics of these Gaussian distribution datasets. Notable variations are observed in the M_v of the *CBGs*. The maximum and minimum *CBG* areas, 1.84 and 0.456 mm^2, respectively, are recorded at 0 and 50 Hz. Subsequently, the M_{ed} experiences a marginal increment to 0.56 mm^2 at 80 Hz, followed by further elevations to 0.624 mm^2 at 110 Hz. Likewise, the C_d reflects a parallel trend with the M_v. In the 0 Hz sample, the C_d registers at 2.672 mm^2, subsequently decreasing to 0.464 mm^2 at 50 Hz.

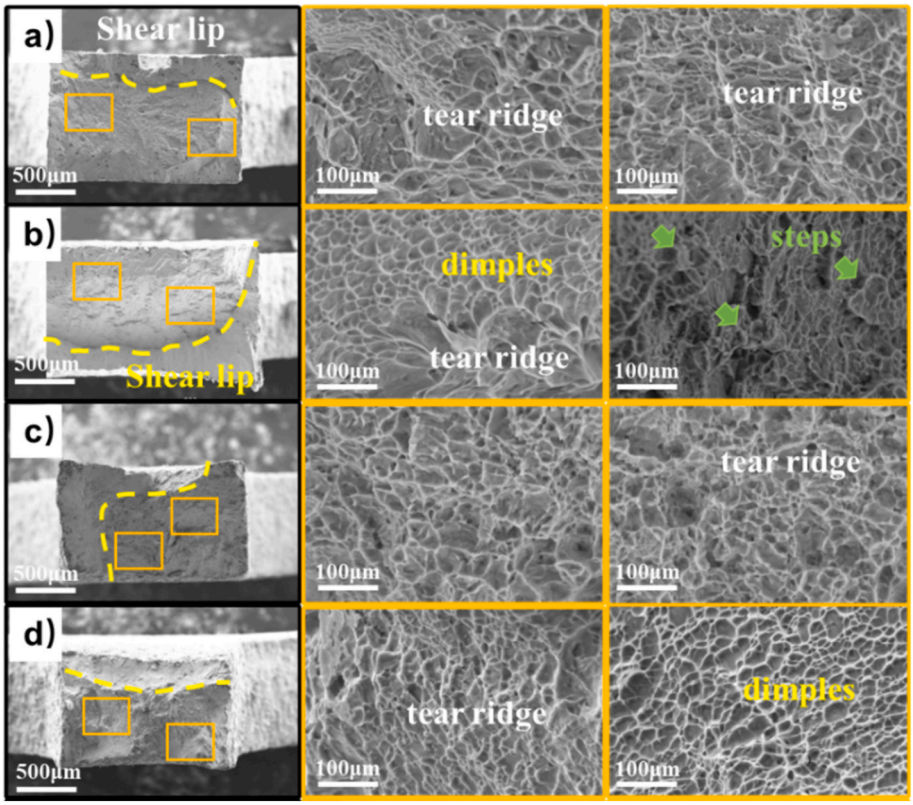

Fig. 5. Fractography under different F_p (Unit: Hz): (a) 0, (b) 50, (c) 80, (d) 110.

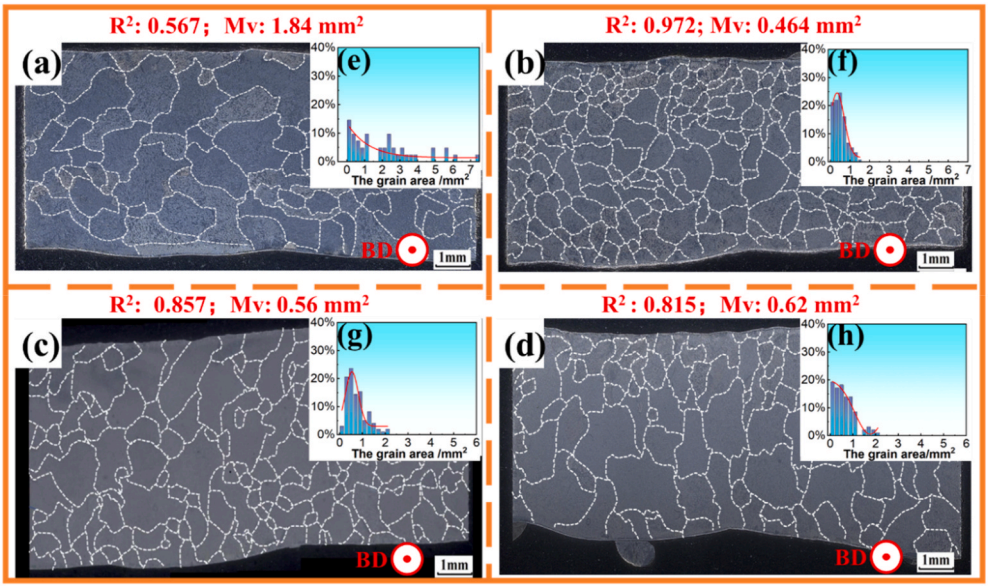

Fig. 6. The morphology images under different F_p (Unit: Hz): (a) 0, (b) 50, (c) 80, (d) 110, and the grain distribution charts under different F_p (Unit: Hz): (e) 0, (f)50, (g) 80, (h) 110.

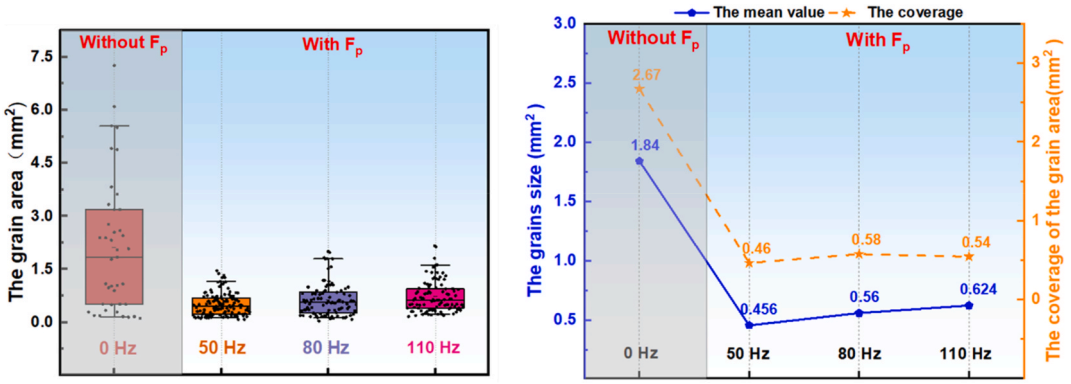

Fig. 7. (a) Grain size distribution boxplot and (b) mean value and concentration degree curves under different F_p.

Following this, the C_d exhibits slight fluctuations around 0.570 mm^2 at 80 Hz and 110 Hz.

These observations underscore the synchronized influence of pulse frequency (F_p) on both the M_v and C_d of *CBGs*. A noteworthy five-fold discrepancy is evident in comparing these values under 0 and 50 Hz, underscoring the substantial impact of current/voltage-impulse cycles on the *CBGs*. Simultaneously, the observed M_v and C_d trend of initially decreasing and subsequently plateauing suggests that the pulse frequency (F_p) of current/voltage-impulse cycles may exhibit an optimal value range conducive to enhanced grain refinement.

3.3. The α-lath structures obtained under different pulse frequencies

The EBSD results, including the SEM figures, Inverse Pole figures (IPFs), and phase figures, are illustrated in Fig. 8. These results reveal the microstructure morphology inside the *CBGs* under different F_p samples. The boundaries of these *CBGs* are distinctly demarcated by the white arrows as depicted in the SEM maps of Fig. 8. Along these *CBG* boundaries, some sub-α structures have a relatively long and narrow shape, denoted as α_{GB}, as the red arrow shown in the Phase map.

The phase maps reveal an exceedingly low presence of sub-micron β inclusions. This phenomenon can be ascribed to the inherent high cooling rate associated with the AM process, which has been previously documented [28,29] in the Ti-alloy. This elevated cooling rate triggers diffusionless and shear-type phase transformations, thereby imparting a distinctive hierarchical α-martensite lath structure to these specimens. In the comparative analysis of the SEM figure, phase figure, and IPF figure presented in Fig. 8, samples subjected to pulse frequencies of 50 and 80 Hz manifest the most diminutive α-lath structures and exhibit the finest α-grain boundaries. Subsequently, the sample was subjected to a 110 Hz follow-up. The specimen subjected to 0 Hz showcases the roughest α-lath dimensions.

Fig. 9 illustrates the microstructural characteristics of the samples subjected to different F_p conditions. Specifically, Fig. 9(a), (e), and (i) display SEM images of the top region of the deposited wall, while Fig. 9 (d), (h), and (m) show SEM images of the bottom region. Fig. 9(b, c), (f, g), and (j, k) correspond to SEM images of the middle section. In the top and bottom regions, the microstructure features basket-weave structures and large-sized α colonies, a consequence of the higher cooling rates dictated by the plate and air conditions in these regions, respectively. Conversely, the middle section exhibits columnar boundary grains (CBGs) (as evidenced in Fig. 9(c), (g), and (k)), resulting from the slower cooling rate in this area. Adjacent to these CBGs boundaries are some large-sized α colony structures. Notably, in samples without F_p (Fig. 9 (b)), a few α colony structures are still present in the middle region. However, such structures are significantly less prevalent in samples subjected to F_p (as shown in Fig. 9(f) and (g)), highlighting a difference in microstructure influenced by the impulse cycles' application. The α

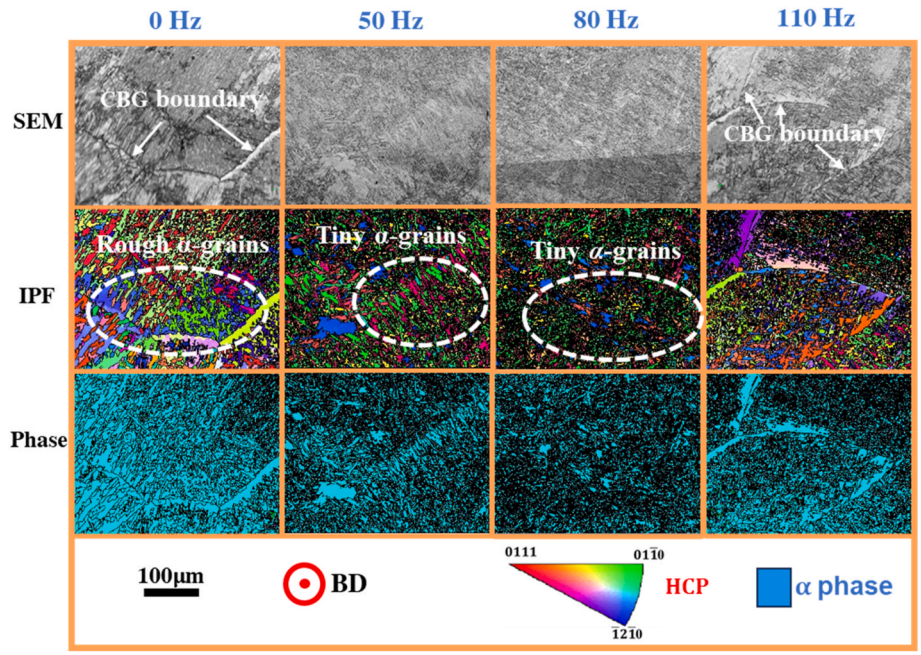

Fig. 8. SEM figure, Inverse pole figure, phase distribution figure of the TA15 samples under different F_p.

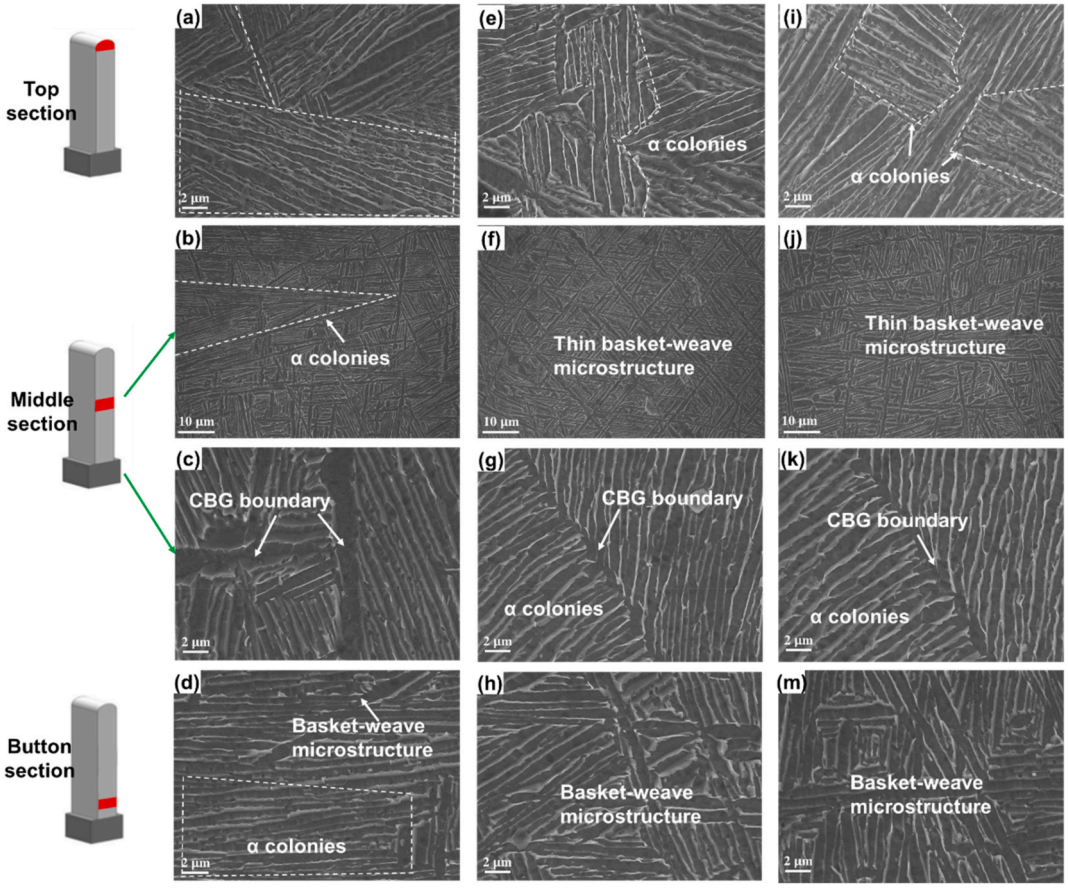

Fig. 9. The microstructure of different WPAAM zone under different F_p (Unit: Hz): (a~d) 0, (e ~ h) 50, (h ~ k) 80.

colonies exhibit a consistent orientation of α-laths, which may undergo similar rotations under external loading conditions. This part will be further discussed in subsequent sections of the analysis.

Fig. 10(a)–(c) illustrate microstructures characterized by a basketweave morphology with acicular α-laths under varying parameters. However, with the introduction of impulse cycles, notable changes in the width of α-laths are observed, as shown in Fig. 10(d)–(f). Statistical analyses presented in Fig. 10(d)–(f) further support these findings.

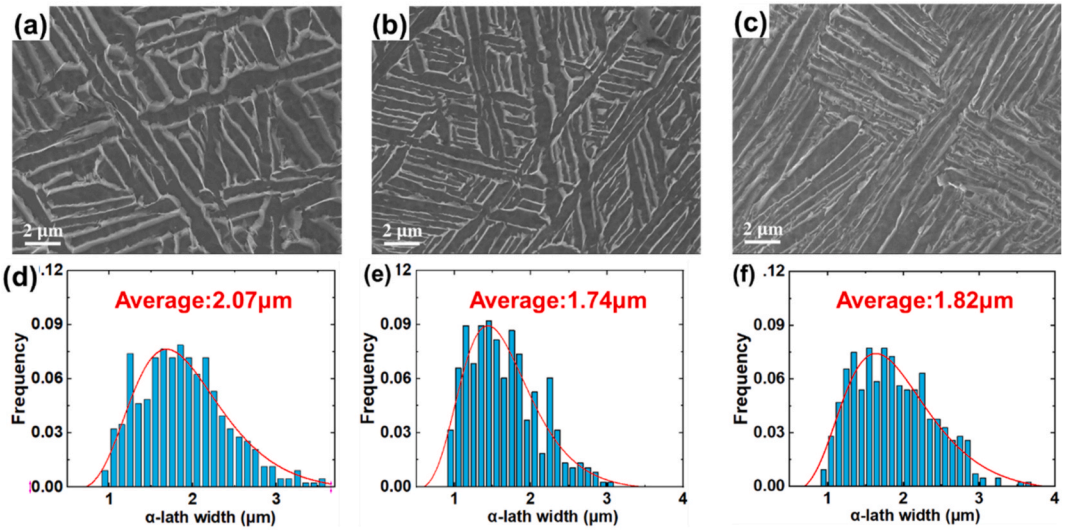

Fig. 10. Microstructural SEM figures under different F_p (Unit: Hz): (a) 0, (b) 50, (c) 80; and corresponding analysis of α-laths width under different F_p (Unit: Hz): (d) 0, (e) 50, (f) 80.

The red lines in these figures denote Gaussian distribution fitting lines, demonstrating fitting confidence levels exceeding 92%. Specifically, the average width decreases from 2.07 μm at 0 Hz to 1.74 μm at 50 Hz, and slightly increases to 1.82 μm at 80 Hz. These observations highlight the impact of impulse cycles on refining the microstructure within α-laths, which may contribute to potential enhancements in the mechanical properties and performance characteristics of the deposited metal.

4. Discussion

4.1. Mechanism of pulse frequency on microstructures

4.1.1. Consideration of the heat input under different parameters

Previous studies [6,8–10] show that solidification textures are mainly determined by the thermal gradient(G) to growth rate(R) ratio (G/R ratio). Therefore, two plausible mechanisms are advanced to explain how F_p may modulate solidification microstructures. Firstly, the alterations in F_p may induce changes in the heat input (HI), thereby influencing the G through the grain growth mechanism and consequentially impacting the solution process. Secondly, F_p may exert an influence on the droplet translation process, thereby modulating droplet frequency and velocity. This modulation, in return, contributes to increasing the R value by augmenting nucleation points, amplifying the solidification ratio.

The heat input (HI) can be calculated using the current and voltage curves obtained by Eqs. (1) and (2).

$$Q = \eta \times \sum (U_i \times I_i \times T_i) \tag{1}$$

$$HI = \frac{Q}{S_t \times T} \tag{2}$$

wherein Q is the total energy caused by the arc, η is the arc thermal efficiency, which is a constant of 0.8 [30] in the CMT method. The values U_i , I_i and T_i are the current values, voltage values, and relative interval time, respectively. The traveling speed (S_t) remains stable across this study, as Table 2 mentioned, which is 0.35 m/min. By Eqs. (1) and (2), the HI can be obtained, the calculations under different F_P are shown in Fig. 11.

Compared with the HI under different F_p, the values exhibit a subtle undulatory fluctuation within the magnitude of 3.25 × 10^5 J/m. This observation suggests a limited susceptibility to alterations concomitant with fluctuations in the F_P. This stable trend may be attributed, in part,

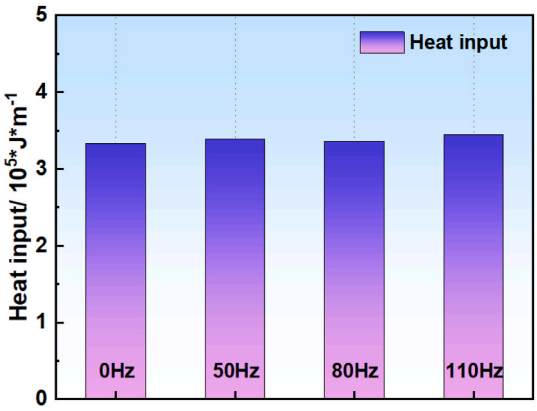

Fig. 11. Heat input (HI) calculation in one CMT circle under different F_p.

to two explicative factors. Firstly, each impulse circle lasts only about 0.5 ms. This transitory span is too brief to impact the HI substantially, according to Eq. (1). Secondly, the WPAAM parameters used in this study are pre-designed programs that restrict the relationship between the current and the wire feeding speed. This makes a balance between the melting material and the heat input. As a result, due to a maintained wire feeding speed, the average current and voltage remain similar across different WAAM processes, as shown in Fig. 2, rendering the HI almost identical.

4.1.2. The kinetic energy in the S/L surface under different pulse frequencies

The G/R ratio is not solely influenced by the HI but also by the kinetic energy distribution amidst the liquid and solidification states, necessitating further analysis. To reveal the mechanism of the pulse frequency changes on the energy fluctuations of the solid-liquid (S/L) interface in the molten pool, a volume of fluid (VOF) model is used to obtain the liquid metal velocity in the S/L interface. However, the S/L interface is located at the rear end of the molten pool, as shown in Fig. 12 (a), making it challenging to calculate accurately. This study introduces a calculation principle aimed at quantifying the motion in the molten pool, which mainly focuses on the aiming area Ω, as shown in Fig. 12 (a), to represent the average kinetic energy obtained on the entire S/L interface.

The vibration energy E_Ω in the S/L interface is expressed in the

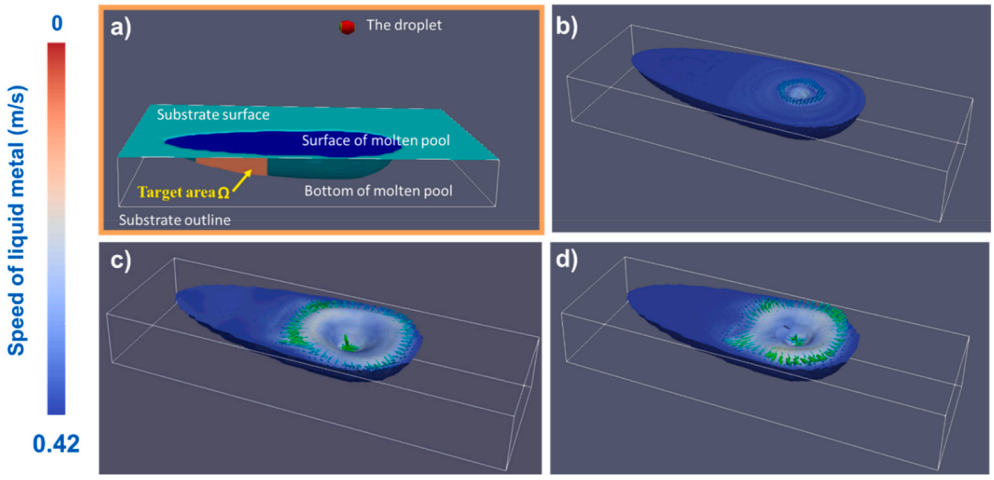

Fig. 12. (a)The VOF calculation principle schematic diagram and (b) to (d) are the initial deformation moments under different F_p (Unit: Hz): (b) 0, (c) 50, (d) 80.

following Eq. (3):

$$E_\Omega = \frac{1}{2}\int_\Omega m_A \left|\overrightarrow{U_A}\right|^2 dA \tag{3}$$

Where the subscript surface is the area element, m_A represent the mass of the liquid metal in the area element, $\left|\overrightarrow{U_A}\right|$ is the average speed in the area element. In addition, the liquid metal in the molten pool can be regarded as homogeneous fluid, which the m_A can be considered as a constant value in the equation. The velocity vector $\overrightarrow{U_A}$ contained three-dimensional weight vector U_x, U_y, U_z, thus Eq. (3) can be rewritten to Eq. (4).

$$E_\Omega = \frac{1}{2} m_A * A * \overline{U}^2 \tag{4}$$

Wherein the $\overline{U}$ represent the average velocity value of the molten pool, which can be re-written by the contribution of the weight velocity vector U_x, U_y, U_z, as following Eq. (5) shows.

$$\overline{U} = \frac{\int_\Omega \left|\overrightarrow{U_A}\right| dA}{\int_\Omega dA} = \frac{\int_\Omega \sqrt{U_x * U_x + U_y * U_y + U_z * U_z}\, dA}{\int_\Omega dA} \tag{5}$$

The initial conditions and boundary conditions of the simulation are shown in Table 3. Fig. 12 (b), (c), and (d) show the initial deformation moments under different F_p. The elements in various colors in these figures denote distinct velocities. With the impact of the droplets, the molten pool causes a significant deformation. As shown in Fig. 12, the molten pool deformation at 0 Hz is much slighter than that at 50 and 80 Hz.

Fig. 13(a)–(c) depict a single-droplet impact circle at the F_p of 110 Hz. In Fig. 13 (c), the impact of droplets engenders a profound deformation in the molten pool, leading to the fluctuation in the elements present in varying directions. Furthermore, as depicted in Fig. 13 (d)–(f), another instance of a single-droplet impact circle in the molten pool is illustrated. During this period, the deformation that occurred by the droplet drove the liquid metal to propagate toward the tail end. This, thereby, increases the metal flow velocity at the S/L surface, as shown in Fig. 14 (e) and (f). The average speed in the aiming plane Ω and the kinetic energy under different parameters are presented in Fig. 14 (a) and (b), respectively. The peak velocity without Fp is much lower than that with Fp, as shown in Fig. 14 (a). Therefore, the kinetic energy without F_p is much lower than that with F_p.

Comparing the liquid metal speed under different F_p, it is not difficult to see that as the F_p increases, the droplet transfer frequency per unit time increases significantly. The frequency of the peak speed in Fig. 14 (a) will also decrease with the droplet transfer frequency increasing, accordingly. However, since the wire feed speeds used in this article are entirely equal, as shown in Table 1, the size of the droplet will become smaller as the droplet transition frequency increases. As a result, the deformation produced in the molten pool also decreases, as shown in Fig. 12, and the resonance amplitude generated in the S/L interface will also weaken. This explains why the peak value of the average velocity in the target area Ω decreases accordingly with the F_p increasing, diminishing from approximately 0.0104 m/s at 50 Hz to 0.0064 m/s at 80 Hz and then decrease to 0.0015 m/s at 110 Hz.

Furthermore, in order to get the synergistic effect of the droplet transfer frequency and the peak value of the average velocity in the S/L interface, the cumulative value of kinetic energy in the target area Ω within 180 ms is counted. The kinetic energy within the area Ω is calculated by Eqs. (4) and (5), shown in Fig. 14 (b). The results show that the kinetic energy without impulse cycles is very low, only 0.0442 × 10^{-3} m^2/s^2. When the pulse frequency is 50 Hz, the kinetic energy is 0.668 × 10^{-3} m^2/s^2, approximately 15 times higher than without impulse cycles. Then, as the pulse frequency increases, the kinetic energy in the target area Ω decreases, at 0.229 × 10^{-3} m^2/s^2 and 0.118 × 10^{-3} m^2/s^2 when the F_p is 80 Hz and 110 Hz, respectively. However, even with the minimum kinetic energy in the samples with impulse cycles, the energy at 110 Hz is still 2.7 times than that without impulse cycles.

Table 3
The initial conditions and boundary conditions of the numerical simulations.

Simulation Conditions	Value
The density of liquid metal (kg/m^3)	4500
The initial velocity of the droplets	0.94 m/s [31]
The arc force	2.73*10^{-3} N [32]
The viscosity of liquid (kg/m*s)	5.2 × 10^{-3}
The length of the molten pool (mm)	8
The width of the molten pool (mm)	5.7
The depth of the molten pool (mm)	2

4.1.3. The mechanism of impulse cycles effect on the microstructure

Combined with the experimental results Figs. 6–8 and simulation results Figs. 12–14, the mechanism of the influence of impulse cycles on microstructure is further explained. The microstructure mechanism diagram with and without impulse cycles is shown in Fig. 15. Fig. 15 (a) describes the WPAAM process, in which, due to the consistency of the temperature gradient G in heat dissipation from the bottom to the top, the deposited metal is easily nucleated to produce bottom-up columnar crystals (CBGs), which is already being studied by the previous researches [16,17,25–27]. Fig. 15(b) and (c) show the solidification

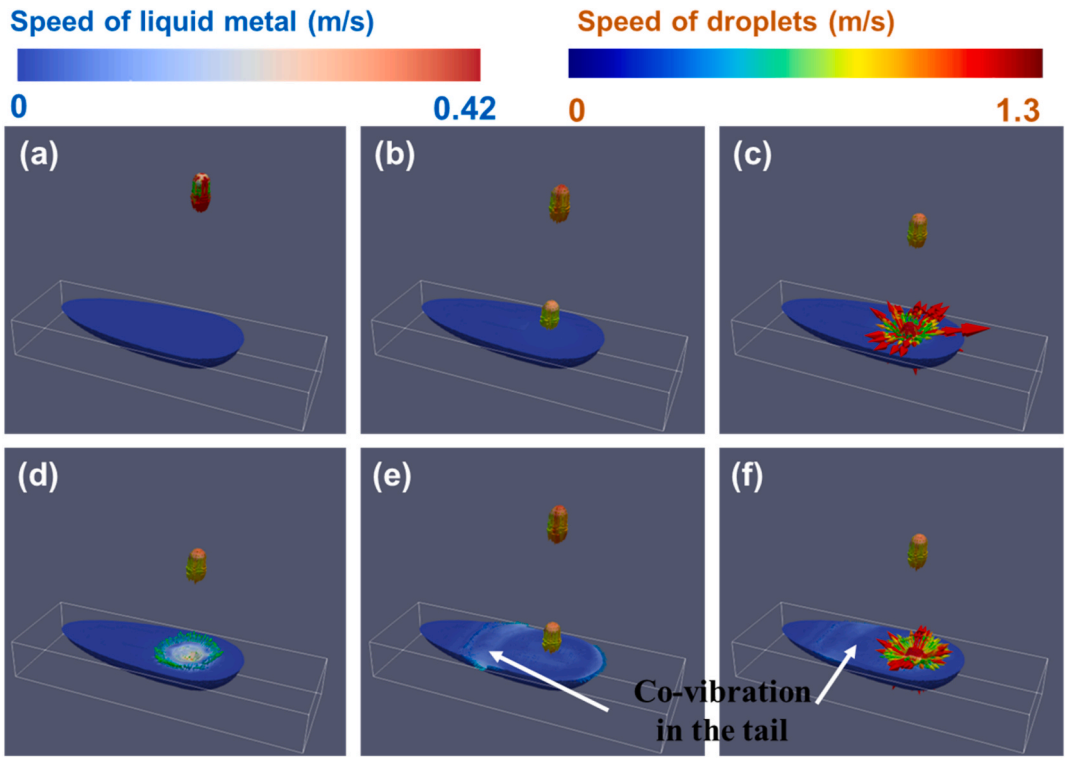

Fig. 13. Two droplet circles under 110 Hz (unit: ms): (a) 0, (b) 10, (c) 12, (d) 14, (e) 20, and (f) 22.

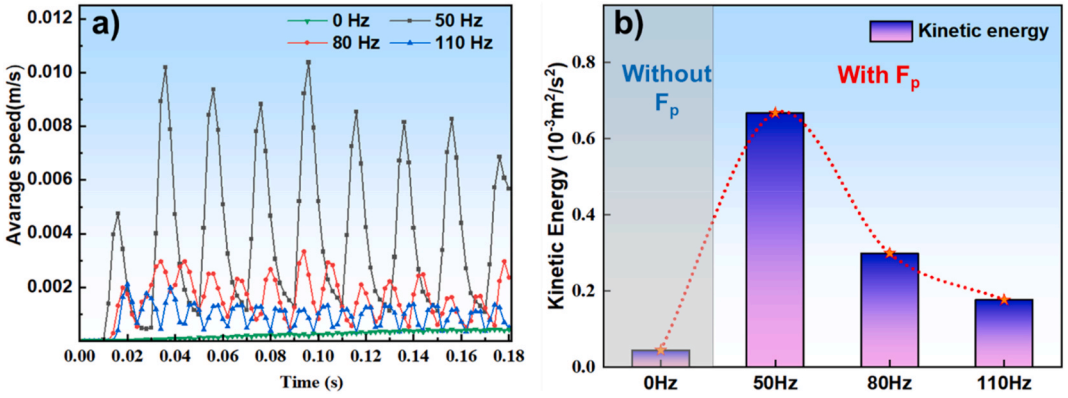

Fig. 14. (a) Average speed in the aiming area (Ω) under different F_p and (b) Integration results of the average speed square.

process of CBGs on the S/L interface with and without impulse cycles, respectively.

When subjected to droplet impact, the molten pool undergoes deformation in the dropping point, as shown in Fig. 12. The deformation in the molten pool forces the liquid metal to move toward the tail end, causing vibration in the molten pool. However, due to the damping effect of the liquid metal in the molten pool, the oscillatory flow of the liquid metal will gradually slow down during the transfer process. Therefore, when there are no impulse cycles, the amplitude of the molten pool oscillation caused at the dropping point is low (this can be found in Fig. 12(b)), which makes this oscillation unable to be transmitted to the S/L interface under the damping effect of liquid metal, as shown in Fig. 15 (b). As a result, the CBGs will continue to grow to a large size, which explains why CBGs' sizes are so big in Figs. 6(a) and 7 (a).

On the other hand, when there are impulse cycles in the parameters, the amplitude of the molten pool oscillation caused at the dropping point is large, which can be found in Figs. 12 (c), (d), and 13 (d). This makes the vibrational oscillations induce a perturbation at the *S/L* interface, as shown in Fig. 15 (c). These vibrational oscillations render the *CBGs* along the *S/L* interface predisposed to fracturing. Then, the tiny CBGs formed by the breakage steps serve as nucleation core, instigating the genesis of other CBGs. This explains why the CBGs with impulse cycles are relatively smaller than those without impulse cycles. The breakage steps also point out the reason why the distribution pattern of *CBGs* aligns exceedingly well with the GS distribution in Fig. 6 (f), (g), (h). Furthermore, the kinetic energy of the *S/L* interface is larger in samples under 50 Hz compared to 80 Hz and greater in turn compared to samples under 110 Hz. This leads to an opposite pattern in the distribution of CBGs, which is smallest under 50 Hz, followed by 80 Hz, and largest under 110 Hz, fitting the CBGs trend in Fig. 7 (b).

In addition, with the velocity in the S/L interface changing, the transduction of energy in this interface also changes, thereby influencing the growth rate R. As per [33,34], the elevated R, in the AMed process, instigates the formation of diminutive α laths. This phenomenon elucidates the observed diminutiveness of α laths nestled within *CBGs* in

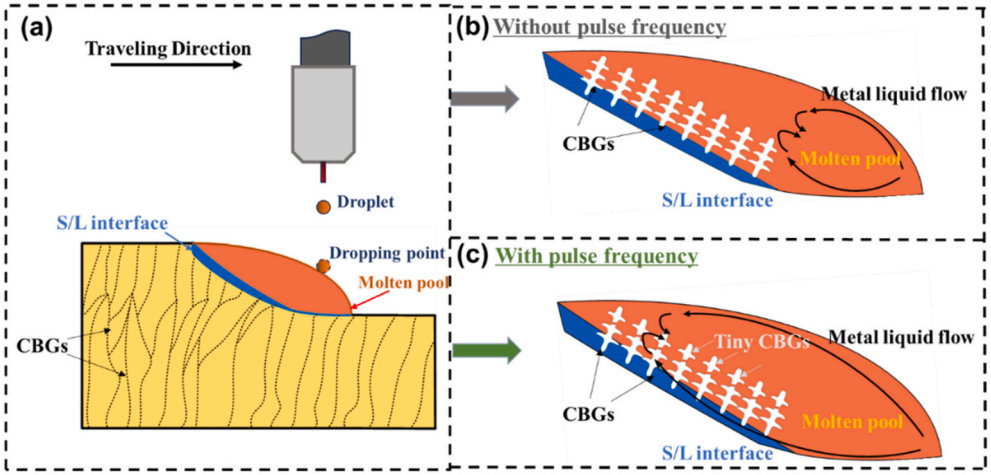

Fig. 15. The microstructure mechanism diagram without and with impulse cycles.

instances of 50 Hz and 80 Hz, as delineated in Fig. 8. In contrast, the sample under 0 Hz and 110 Hz have a comparatively diminished fluidic flow magnitude at the S/L interface. This concomitantly results in a relatively lower R, thereby engendering the coarsening of the α grain structures. Furthermore, the growth rate direction also changes the α laths' growth direction. As shown in Fig. 15 (b), without the fluctuation in the S/L, the α laths' growth direction follows the building direction, as the growth rate direction along the building direction. On the contrary, with the liquid metal flow effect, the heat exchange process is disrupted, which offsets the growth rate direction relative to the building direction. This makes the α laths' growth in more directions and reduce the α colony structures, as shown in Fig. 9.

4.2. Correlation between microstructure and yield strength of TA15-alloy

4.2.1. The contribution of CBGs on yield strength

In the mechanical results shown in Fig. 4, the *YS* and *UTS* have a contrasting co-relationship with the *CBGs* size curve reported in Fig. 6. This indicates that the tensile strength corresponding with the *CBGs* mentioned previously. The observed enhancement in strength can be partially attributed to the distribution of the *CBGs*. During the tensile test, the deformation in the tensile sample is exerted on multiple grains. Therefore, refined grains can reduce stress concentration. The Hall-Petch (*H–P*) relationship [35] can explain such an effect, illustrating that the δ_{ys} is inversely proportional to the *d*. In the AMed titanium alloy, the CBGs attain a coarser scale. The previous study [36] proposes a modified *H–P* relationship to improve calculation accuracy by illustrating the width of the *CBGs* and the *YS*, as Eq. (6) shows.

$$\delta_{ys} = \delta_0 + \frac{k_y}{\sqrt{w}} \tag{6}$$

wherein the δ_0 is denoted a material constant representing the initial resistance to dislocation movement, k_y signifies the strengthening coefficient, a constant parameter specific to the given material, and *w* is the average width of the *CBGs*. According to the study [36], for AMed TA15 alloy, the δ_0 and k_y are 710 MPa and 3.31 MPa/m$^{-1/2}$, respectively.

To get the accurate grain width, the average *CBGs* width of the metallographic samples can be calculated by the grain areas shown in Figs. 6 and 7, in which the single *CBG* can be approximately considered a regular hexagon. The diameters of the inscribed circle inside the hexagons can represent the width of the *CBGs*, which can be deduced by the following Eq. (7).

$$d_{avg} = \sqrt{\frac{2}{\sqrt{3}} A_{avg}} \tag{7}$$

wherein the A_{avg} is the average grain area from Fig. 7 (b), the d_{avg} is the diameter of the inscribed circle of the hexagon that wanted to be counted out.

From the H–P relationship in Eq. (6) and the estimated width d_{avg} by Eq. (7), the estimated YS of the samples under different Fp can be calculated, as shown in Table 4. With the CBGs' average width decreased, both the experimental and calculated YS in Table 4 ascents. The tendency of the calculated results closely approximates the experimental findings, which are also inversely proportional to the CBG's average width. However, a significant estimated error by at least 90 MPa existed between the experiment and H–P calculation results. This disparity can be attributed to the fact that the WAAMed parts feature large CBG boundaries. The dislocation movement effect by these CBG's boundaries is minimal, implying that the H–P effect cannot be satisfied with such coarse grains.

4.2.2. The contribution of α-grains on yield strength

As shown in Figs. 9 and 10, with the introducing of the impulse cycles, the α-grains' width inside the CBGs also change correspondingly. This may also contribute to the strength of the deposited metal. Fig. 16 shows the Taylor factors (T.F.) distribution figure, Kernel average misorientation (KAM) figure, and KAM distribution chart obtained via EBSD. The T.F. value indicates how easily the grain may undergo rotation. The larger T.F. value implies the increased difficulty in grain rotation. Thus, the T.F. figure delineates the prospect of grain rotation under external loading. Notably, the specimens subjected to 50 and 80 Hz are characterized by the most diminutive α-laths (as shown in Figs. 8–10), having some interweaving texture. In the T.F. map, this interweaving texture manifests as a microstructural matrix intricately rearranged by certain 'hard' α-laths within some 'soft' α-laths. These rearrangements, moreover, afford a robust defense against deformation under external loads. On the contrary, the samples at 0 Hz exhibit the stubbiest α-laths matrix. Fewer microstructural rearrangements can be found in these samples, signifying that the materials in these sections are relatively easy to rotate and yield. This proves that the basketweave-like *α*-laths inside the *CBGs* also may play a pivotal role in yield strength.

The KAM figures under different F_p also show that the α-structure plays an important role in deformation, with blue denoting the lowest

Table 4
The experimental and calculated *YS* under different parameters.

F_p (Hz)	0	50	80	110
The experimental *YS*/MPa	888.48	1007.58	987.64	941.45
The calculated *YS*/MPa	793.7761	829.822	823.0034	819.4286
Error/MPa	94.7039	177.758	164.6366	122.0214

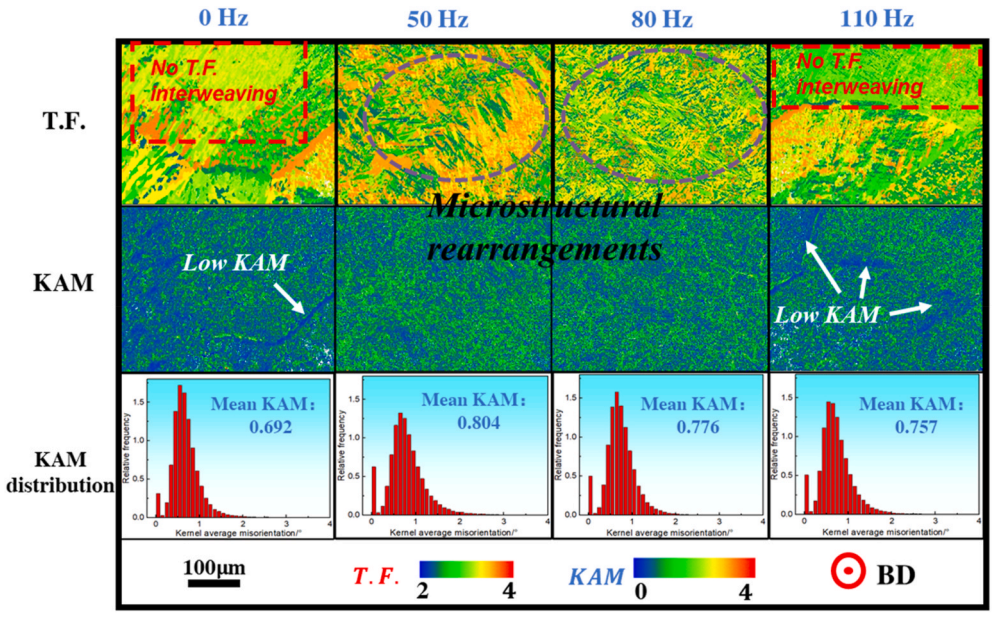

Fig. 16. Taylor factors distribution figure, KAM figure, and KAM distribution chart of the TA15 alloy samples under different F_p.

value (0°) and red denoting the highest value (4°). As the KAM distribution chart is shown in Fig. 16, the 50 and 80 Hz samples exhibited the highest KAM values, succeeded by the 110 Hz sample, then a subsequent decline in the 0 Hz samples.

Due to the close relationship between KAM and Geometrically Necessary Dislocations (GNDs) [37,38], the GND density can be calculated using equation (8):

$$\rho_{GND} = \frac{2\theta_{KAM}}{\mu b} \tag{8}$$

Where ρ_{GND} is the GND density; θ_{KAM} represents the local misorientation in the KAM maps [37]; b is the magnitude of the Burgers vector [39]; μ is the kernel size [40], which can be calculated by $\mu = cl$, where c is the nearest neighbor determined in the program and l is the scan steps via EBSD. Thus, the KAM value directly determines the distribution of GND density. Indeed, the higher the KAM value, the larger the GNDs density, signifying a more potent hindrance to the action of external forces.

Thus, in order to consider the α-laths inside the *CBGs,* Schmid law is used to judge the contribution of α-laths to the *YS*. Schmid law explains that the improvement of *YS* under statistic loading can be attributed to the dislocation slips in plastic deformation of the solidification textures. As per the Schmid law [41], the relationship between the yield strength δ_Y and the Schmid factors *SF* can be expressed as follows:

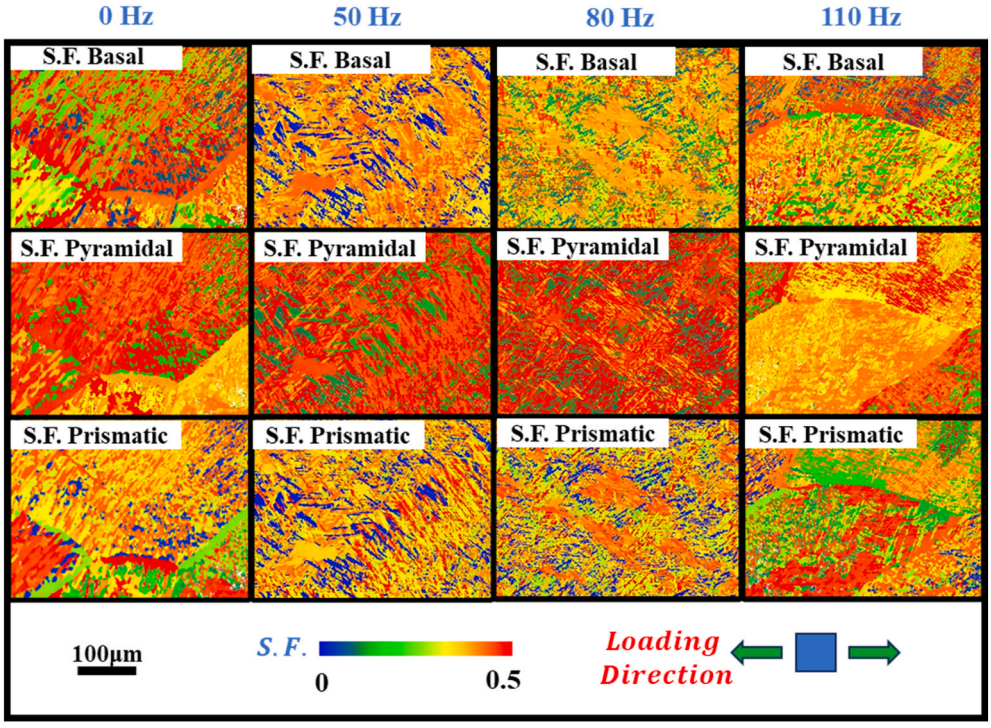

Fig. 17. Schmid factors maps on the basal, pyramidal, and prismatic planes of the TA15 alloy samples under different F_p.

$$\delta_{ys} = \frac{\zeta^{CRSS}}{SF} \tag{9}$$

where ζ^{CRSS} is the critical resolved shear stress for the material. As for the critical resolved shear stress (ζ^{CRSS}), different phases and slip systems have different values.

As shown in the Phase maps from Fig. 8, the majority of the components in TA15 samples are α phase, which means the α phase plays a leading role in the metal slip process. The α phase in titanium alloys accommodates three distinct slip systems, denominated as basal slip system ($\{0001\} < 11\bar{2}0 >$), prismatic slip system ($\{1\bar{1}00\} < 11\bar{2}0 >$) and pyramidal slip system ($\{10\bar{1}1\} < 11\bar{2}0 >$) or ($\{10\bar{1}1\} < 11\bar{2}3 >$), respectively. Fig. 17 presents Schmid factors distribution maps upon these three slip systems, with blue denoting the lowest value (0) and red denoting the highest value (0.5). The loading direction of Schmid factors is set along the transverse direction of the sample, as shown in Fig. 17.

Fig. 18 (a) to (c) delineate the Schmid factors distribution maps corresponding to the basal, prismatic, and pyramidal slip planes. Notably, within these three slip systems, all samples exhibit the highest Schmid factors on the pyramidal slip system, as shown in Fig. 18 (c). However, previous studies [42–44] posit a markedly greater critical resolved shear stress ζ^{CRSS} of the pyramidal slip system compared to the basal and prismatic slip system. Consequently, although the considerable Schmid factors are associated along the pyramidal slip system, this slip system is difficult to activate at the initial stages of plastic deformation.

From the distributions of the Schmid factor under different F_p, average Schmid factors can be calculated by Eq. (10).

$$\overline{m} = \frac{\int m \times N(m) dm}{\int N(m) dm} \tag{10}$$

Wherein the $N(m)$ is the frequencies of the α phase and m is the Schmid factors of the α phase corresponding to the determining slip system. By calculation, the average Schmid factors $\overline{m}$ results are shown in Table 5.

The ζ^{CRSS} pertinent to the basal and prismatic slip systems within titanium alloys exhibits a similarity value. Reported ζ^{CRSS} from the previous literature are listed in Table 6. The ζ^{CRSS} used in this study are 365 MPa and 345 MPa for the basal and prismatic slip systems, respectively.

4.2.3. The joint contribution of CBGs and α laths on yield strength

By using the Schmid law along with the ζ^{CRSS} and $\overline{m}$ values mentioned previously, the theoretical estimations can be calculated. The calculation results by prismatic slippage and basal slippage are depicted in Fig. 19, represented as the black and purple lines, respectively. The theoretical estimations derived from the *H–P* relationship of *CBGs* width are also illustrated in this figure, as the blue line shows. The red dashed line within Fig. 19 delineates the experimentally derived yield strength.

Table 5
The average Schmid factor.

F_p (Hz)	0	50	80	110
$\overline{m_{basal}}$	0.345536	0.310748	0.315656	0.340847
$\overline{m_{pris}}$	0.363293	0.330031	0.33291	0.351552

Table 6
The ζ^{CRSS} reported in the previous studies.

Materials	ζ^{CRSS} (MPa)		Reference
	Basal slip	Prismatic slip	
Ti6Al4V	388	373	[45]
Ti6Al4V	400	380	[46]
Ti6Al4V	420	370	[47]
Ti6Al2Sn4Zr2Mo	365	345	[48]
Ti6.5Al2ZrMoV	365	345	This study

In Fig. 19, the experiment and Schmid law analysis lines reveal that the *YS* exhibits an upward trend from 0 Hz to 50 Hz and has a slight downward trend from 50 Hz to 110 Hz. The experimental *YS* results are higher than those calculated from H–P and are much lower than those calculated from basal SFs. The *YS* results calculated by prismatic SFs are the closest to the experimental *YS*, with a maximum error of only 61 MPa.

However, it can also be seen from Fig. 19 that the results calculated by prismatic SFs are always slightly higher than the experimental values among these four samples. This implies that relying solely on one theoretical method to elucidate the yield strength in the WPAAM process is not comprehensive. Concurrently, certain α colony structures adjacent to the *CBGs*' boundaries are discerned in Figs. 8 and 9. Because the energy required for non-uniform nucleation is much less than the energy required for uniform nucleation, the α colony structures preferentially precipitates at the CBG boundary, as shown in Fig. 9. These α colony structures portray a relatively diminished KAM value, as shown in Fig. 16, which are easily activated and causes slippage. This also shows the contribution of *CBGs*' boundaries to mechanical properties. In conclusion, the observation underscores the interplay of solidification textures, encompassing both the structure of *CBGs* and the structure of α-laths, imparting a distinctive mechanical response to WPAAMed Ti-alloys.

5. Conclusions

In this study, several noteworthy conclusions can be drawn based on the microstructure and mechanical properties under varying parameters.

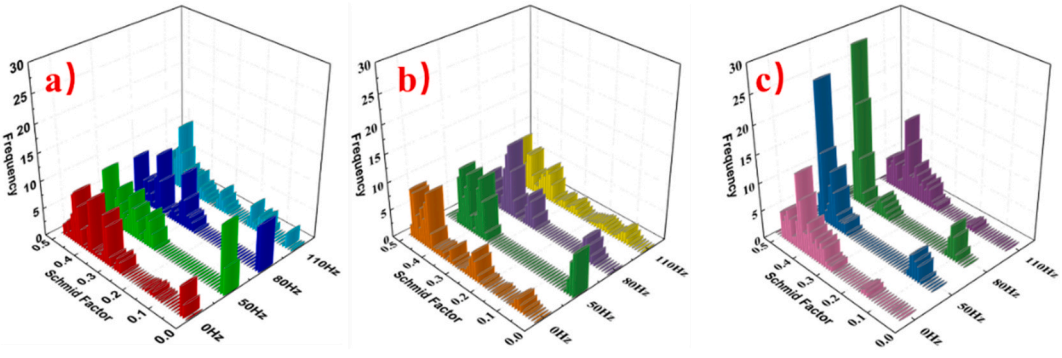

Fig. 18. Schmid factors distribution of the TA15 alloy samples under different F_p, (a) on the basal planes, (b) on the pyramidal planes, and (c) on the prismatic planes.

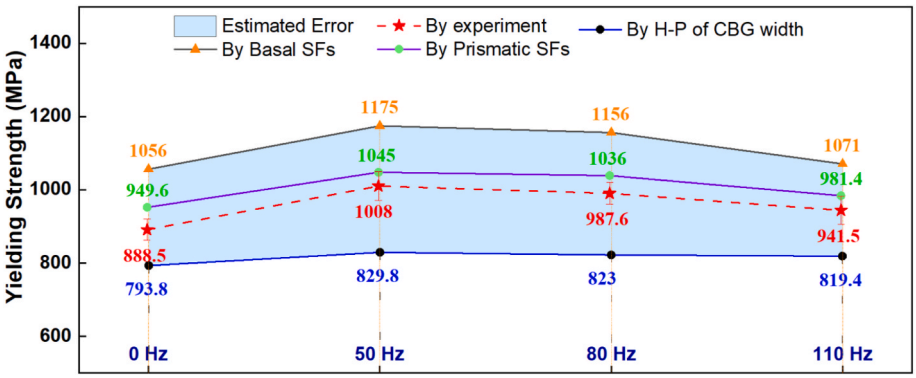

Fig. 19. Correlations between yielding strength, CBGs and the α-laths.

1. The analysis of yield strength improvement involved the application of the Hall-Petch relationship and Schmid Law. The examination revealed that the CBGs and the α-phase texture collectively contribute to the observed enhancements in mechanical properties.
2. The droplets' kinetic energy dominates the distribution of the CBGs. As the peak value of kinetic energy at the S/L interface increases, the probability of CBG breakage rises, resulting in a more aligned distribution of CBGs resembling a Gaussian distribution.
3. The co-vibration occurring at the solid/liquid interface acts as a facilitator for energy transduction, exerting an influence on the growth rate and altering the growth direction of the α grains cluster. This phenomenon contributes to the initiation of diminutive α grains, marking a distinctive effect on the overall grain formation process.
4. Compared with the conventional WAAM sample, the samples subjected to the WPAAM have a significant improvement in tensile strength. Optimal process parameter adjustments result in a substantial 13% improvement in both yield strength and ultimate tensile strength.

The WPAAM technology presents a novel alternative for the production of titanium alloys. This method is characterized by its simplicity, as it does not entail additional steps, necessitate special path planning, or require intricate procedures. The inherent ease of implementation makes it particularly well-suited for printing large components. This approach streamlines the manufacturing process and eliminates the need for subsequent post-processing or interlayer interventions. Consequently, it enhances the feasibility of utilizing WAAM components in industrial applications, facilitating the more convenient production of large titanium alloy components.

CRediT authorship contribution statement

Zhenyu Yu: Conceptualization, Experiment, Data curation, Methodology, Software, Investigation, Visualization, Writing-review & editing. Shengfu Yu: Funding acquisition, Methodology, Resources, Supervision, Project administration, Writing-review & editing. Mingwang FU: Funding acquisition, Methodology, Supervision, Investigation, Data curation & editing. Guozhi Yu: Conceptualization, Experiment, Data curation.

Declaration of competing interest

The authors declare that they do not have any commercial interests or personal relationships that could have appeared to influence the work reported in this paper.

Acknowledgements

The authors acknowledge the funding supported by the National Key R&D Program of China (2202YFB4602300) and the Stable Support Project by the Key Laboratory of High Energy Beam Processing Technology. The authors acknowledge the projects from The Hong Kong Polytechnic University [1-W20V, 1-ZE1W and 1-CD4H], and the projects from the General Research Fund of Hong Kong Government [15228621, 15229922 and C4074-22G]. In addition, M.W. Fu would like to thank the Royal Society Wolfson Visiting Fellowship project of RSWVF\R2\222005 to support this research.

References

[1] Flower HM. High performance materials in aerospace. Springer Science & Business Media; 2012.
[2] Qi HB, Ren DL, Zheng MJ. Research on forming technology of electron beam selective melting for Ti-6Al-4V powder. In: Applied mechanics and materials. Trans Tech Publ; 2011.
[3] Lin Z, Song K, Yu X. A review on wire and arc additive manufacturing of titanium alloy. J Manuf Process 2021;70:24–45.
[4] Widomski C, Solas D, Brisset F, Helbert AL, Baudin T, Lebel S. Study of the microstructure and mechanical properties obtained by Laser Boost in SLM process for the Ti-64 alloy. In: Materials science forum. Trans Tech Publ; 2021.
[5] Yu R, Yu S, Yu Z, Zheng B. Directed energy deposition-arc of thin-walled aerobat shell with structures of internal ribs and overhanging gaps. Int J Adv Des Manuf Technol 2023;127(1):305–21.
[6] Khorasani M, Ghasemi A, Rolfe B, Gibson I. Additive manufacturing a powerful tool for the aerospace industry. Rapid Prototyp J 2022;28(1):87–100.
[7] Zhuo Y, Yang C, Fan C, Lin S, Chen Y, Chen C, Cai X. Grain refinement of wire arc additive manufactured titanium alloy by the combined method of boron addition and low frequency pulse arc. Mater Sci Eng, A 2021;805:140557.
[8] Al-Bermani SS, Blackmore ML, Zhang W, Todd I. The origin of microstructural diversity, texture, and mechanical properties in electron beam melted Ti-6Al-4V. Metall Mater Trans A 2010;41A(13):3422–34.
[9] Nie P, Ojo OA, Li Z. Numerical modeling of microstructure evolution during laser additive manufacturing of a nickel-based superalloy. Acta Mater 2014;77:85–95.
[10] Carroll BE, Palmer TA, Beese AM. Anisotropic tensile behavior of Ti–6Al–4V components fabricated with directed energy deposition additive manufacturing. Acta Mater 2015;87:309–20.
[11] Sharma S, Joshi SS, Pantawane MV, Radhakrishnan M, Mazumder S, Dahotre NB. Multiphysics multi-scale computational framework for linking process–structure–property relationships in metal additive manufacturing: a critical review. Int Mater Rev 2023;68(7):943–1009.
[12] Szost BA, Terzi S, Martina F, Boisselier D, Prytuliak A, Pirling T, Hofmann M, Jarvis DJ. A comparative study of additive manufacturing techniques: residual stress and microstructural analysis of CLAD and WAAM printed Ti–6Al–4V components. Mater Des 2016;89:559–67.
[13] Yang J, Yu H, Yin J, Gao M, Wang Z, Zeng X. Formation and control of martensite in Ti-6Al-4V alloy produced by selective laser melting. Mater Des 2016;108:308–18.
[14] DebRoy T, Wei H, Zuback J, Mukherjee T, Elmer J, Milewski J, Beese AM, Wilson-Heid Ad, De A, Zhang W. Additive manufacturing of metallic components–process, structure and properties. Prog Mater Sci 2018;92:112–224.
[15] Körner C. Additive manufacturing of metallic components by selective electron beam melting—a review. Int Mater Rev 2016;61(5):361–77.
[16] Mereddy S, Bermingham MJ, StJohn DH, Dargusch MS. Grain refinement of wire arc additively manufactured titanium by the addition of silicon. J Alloys Compd 2017;695:2097–103.
[17] Jin P, Liu Y, Sun Q. Evolution of crystallographic orientation, columnar to equiaxed transformation and mechanical properties realized by adding TiCps in wire and arc additive manufacturing 2219 aluminum alloy. Addit Manuf 2021;39:101878.

[18] Lu B, Cui X, Ma W, Dong M, Fang Y, Wen X, Jin G, Zeng D. Promoting the heterogeneous nucleation and the functional properties of directed energy deposited NiTi alloy by addition of La2O3. Addit Manuf 2020;33:101150.
[19] Chen X, Su C, Wang Y, Siddiquee AN, Sergey K, Jayalakshmi S, Singh RA. Cold metal transfer (CMT) based wire and arc additive manufacture (WAAM) system. J Surf Investig: X-ray, Synchrotron Neutron Techn 2018;12:1278–84.
[20] Koli Y, Aravindan S, Rao P. Influence of heat input on the evolution of δ-ferrite grain morphology of SS308L fabricated using WAAM-CMT. Mater Char 2022;194:112363.
[21] Wang J, Zhao Z, Du W, Bai P, Wang L, Zhang Z, Huang Z, Liu Y. Uniaxial compression deformation and fracture mechanism of cold metal transfer (CMT) arc additive Mg–Gd–Y–Zn–Zr alloy. Mater Sci Eng, A 2023;878:145201.
[22] Gao Z, Li Y, Shi H, Lyu F, Li X, Wang L, Zhan X. Microstructure characteristics under varying solidification parameters in different zones during CMT arc additive manufacturing process of 2319 aluminum alloy. Vacuum 2023;214:112177.
[23] Wang Y, Li M, Yang X, Zuo H. Effect of P-MIG and CMT on microstructure and properties of 6082-T6 joints. Mater Sci Technol 2023;39(15):2074–89.
[24] Zhang L, Wang S, Wang H, Wang J, Wang T, Dai X. Investigate the effect of arc characteristic on the mechanical properties of 5A56 Al alloy in CMT arc additive manufacturing. CIRP J Manuf Sci Technol 2023;40:102–13.
[25] Bai X, Colegrove P, Ding J, Zhou X, Diao C, Bridgeman P, roman Hönnige J, Zhang H, Williams S. Numerical analysis of heat transfer and fluid flow in multilayer deposition of PAW-based wire and arc additive manufacturing. Int J Heat Mass Transfer 2018;124:504–16.
[26] Bermingham MJ, Nicastro L, Kent D, Chen Y, Dargusch MS. Optimising the mechanical properties of Ti-6Al-4V components produced by wire plus arc additive manufacturing with post-process heat treatments. J Alloys Compd 2018;753:247–55.
[27] McAndrew AR, Rosales MA, Colegrove PA, Hönnige JR, Ho A, Fayolle R, Eyitayo K, Stan I, Sukrongpang P, Crochemore A. Interpass rolling of Ti-6Al-4V wire+ arc additively manufactured features for microstructural refinement. Addit Manuf 2018;21:340–9.
[28] Gwak M, Kim S, Lee DJ, Seol JB, Sung H, Nam T-H, Kim S, Kim JG. Post-annealing effect on the tensile deformation mechanism of a Ti–6Al–4V alloy manufactured via directed energy deposition. Mater Sci Eng, A 2022;836:142729.
[29] Xu W, Brandt M, Sun S, Elambasseril J, Liu Q, Latham K, Xia K, Qian M. Additive manufacturing of strong and ductile Ti–6Al–4V by selective laser melting via in situ martensite decomposition. Acta Mater 2015;85:74–84.
[30] Dupont JN, Marder AR. Thermal efficiency of arc welding processes. Welding J-Includ Weld Res Suppl 1995;74(12):406s.
[31] Zhao W, Jin H, Du X, Chen J, Wei Y. A 3D arc-droplet-molten pool integrated model of Al alloy GMAW process: heat transfer, fluid flow and the effect of external magnetic field. Vacuum 2022;202:111129.
[32] Yang M, Li L, Qi B, Zheng H. Arc force and shapes with high-frequency pulsed-arc welding. Sci Technol Weld Join 2017;22(7):580–6.
[33] Zhu S, Yang H, Guo LG, Fan XG. Effect of cooling rate on microstructure evolution during α/β heat treatment of TA15 titanium alloy. Mater Char 2012;70:101–10.
[34] Su J, Ji X, Liu J, Teng J, Jiang F, Fu D, Zhang H. Revealing the decomposition mechanisms of dislocations and metastable α' phase and their effects on mechanical properties in a Ti-6Al-4V alloy. J Mater Sci Technol 2022;107:136–48.
[35] Bata V, Pereloma EV. An alternative physical explanation of the Hall–Petch relation. Acta Mater 2004;52(3):657–65.
[36] Todaro C, Easton M, Qiu D, Zhang D, Bermingham M, Lui E, Brandt M, StJohn D, Qian M. Grain structure control during metal 3D printing by high-intensity ultrasound. Nat Commun 2020;11(1):142.
[37] Cai W, Wang C, Sun C, Qian L, Fu MW. Microstructure evolution and fracture behaviour of TWIP steel under dynamic loading. Mater Sci Eng, A 2022:851.
[38] Zou Y, Ding H, Zhang Y, Tang Z. Microstructural evolution and strain hardening behavior of a novel two-stage warm rolled ultra-high strength medium Mn steel with heterogeneous structures. Int J Plast 2022:151.
[39] Zhi H, Zhang C, Antonov S, Yu H, Guo T, Su Y. Investigations of dislocation-type evolution and strain hardening during mechanical twinning in Fe-22Mn-0.6C twinning-induced plasticity steel. Acta Mater 2020;195:371–82.
[40] Qiao Y, Chen Y, Cao F-H, Wang H-Y, Dai L-H. Dynamic behavior of CrMnFeCoNi high-entropy alloy in impact tension. Int J Impact Eng 2021;158.
[41] Zhi H, Zhang C, Antonov S, Yu H, Guo T, Su Y. Investigations of dislocation-type evolution and strain hardening during mechanical twinning in Fe-22Mn-0.6 C twinning-induced plasticity steel. Acta Mater 2020;195:371–82.
[42] Benmessaoud F, Cheikh M, Velay V, Vidal V, Matsumoto H. Role of grain size and crystallographic texture on tensile behavior induced by sliding mechanism in Ti-6Al-4V alloy. Mater Sci Eng, A 2020;774:138835.
[43] Liu Z, Zhao ZB, Liu JR, Wang L, Zhu SX, Yang G, Gong SL, Wang QJ, Yang R. Deformation behaviors of as-built and hot isostatically pressed Ti-6Al-4V alloys fabricated via electron beam rapid manufacturing. J Mater Sci Technol 2019;35(11):2552–8.
[44] Li R, Wang H, He B, Li Z, Zhu Y, Zheng D, Tian X, Zhang S. Effect of α texture on the anisotropy of yield strength in Ti–6Al–2Zr–1Mo–1V alloy fabricated by laser directed energy deposition technique. Mater Sci Eng, A 2021;824:141771.
[45] Bridier F, Villechaise P, Mendez J. Analysis of the different slip systems activated by tension in a α/β titanium alloy in relation with local crystallographic orientation. Acta Mater 2005;53(3):555–67.
[46] Dick T, Cailletaud G. Fretting modelling with a crystal plasticity model of Ti6Al4V. Comput Mater Sci 2006;38(1):113–25.
[47] Bridier F, McDowell DL, Villechaise P, Mendez J. Crystal plasticity modeling of slip activity in Ti–6Al–4V under high cycle fatigue loading. Int J Plast 2009;25(6):1066–82.
[48] Venkataramani G, Deka D, Ghosh S. Crystal plasticity based Fe model for understanding microstructural effects on creep and dwell fatigue in Ti-6242. J Eng Mater Technol 2006;128(3):356–65.